Event-based Sensor Noise Modeling for Space-based Space Domain Awareness

Rachel Oliver
Air Force Institute of Technology, 2950 Hobson Way, Wright Patterson Air Force Base, OH 45433
Dmitry Savransky
Cornell University, 124 Hoy Rd, Ithaca, NY 14850

ABSTRACT

Building off the foundation of a physics-based end-to-end model for event-based vision sensors (EVS) observing resident space objects (RSOs), we apply new techniques to model realistic low-light sensor noise. While previous event-generation approaches simulate memorized current leakage and apply temporal noise models, our methods improve on these approaches and additionally account for current-following white noise as an event source. These model improvements are key components for accurate event-generating simulations which can advise requirements and concepts of operations for dedicated event-based Space Domain Awareness (SDA) architectures. An event-generation simulator which models the underlying physics is particularly important for space-based architectures where informative space-based truth data is limited. The EVS pixel's independent and asynchronous recording of changes in photocurrent produces data with high temporal resolution and dynamic range making it an attractive technology for SDA. EVS are particularly appealing as a space-based payload because of their sparse data output reducing the need for downlink, computational, and power resources. To enable creation of a space-based EVS system, our physics-based end-to-end model now includes noise based on induced photocurrent to generate simulated events closer to known truth. We introduce a new Poisson-based method to model the noise generated by the temporal variation of the dark current and a method to tune high-frequency white noise on the induced photocurrent to model the noise on signals above the dark current. These techniques demonstrably improve EVS noise modeling by closely matching observed event rate and polarity behavior, moving EVS one step closer to operational space-based SDA usage.

1. INTRODUCTION

EVS are a promising technology for space-based SDA due to their unique foundational concepts. Biologically inspired EVS detect logarithmic changes in photocurrent on each independent pixel versus a memorized value. The sensor readout is sparse and provides high dynamic range, only reporting the changes that exceed user-set positive and negative current ratios, thresholds. The address event representation readout has high temporal resolution as each pixel asynchronously operates with microsecond level precision. For SDA applications this high temporal resolution enables electro-optical observations of relatively fast moving RSOs. As a result, the technology shows promise to estimate RSO orbits without multiple collections [3]. Combining this with the sparse output representation offers a significant data size optimization versus traditional full-frame integrating sensors. This data optimality may be particularly advantageous to minimize communication link bandwidth requirements for space-based SDA applications and enable on-board processing, with the potential to reduce antenna size and/or power needs. With all of these strengths, EVS continues to be an area of interest to the SDA community, with recent efforts characterizing commercially-available sensor performance for low-light [14, 13], exploring techniques to image RSOs [6, 28], proposing and developing algorithms to process the SDA event data [7, 5, 2, 16, 1, 25, 4, 20], and evaluating space-based capabilities through demonstrations [22, 12]. To further enable space-based applications by providing synthetic events that resemble known truth in event timings and polarities, we propose two new noise modeling techniques for dark current shot noise and high frequency noise for our event generation simulation.

While the simulation we improve in this paper is specifically designed for SDA [21, 19], an event generation simulation, v2e, precedes it and serves as the original inspiration [8]. As a state of the art demonstration tool for EVS, it converts video into idealistic event data streams. Functioning off traditional frame based camera output, the v2e simulation estimates photocurrent change from the digital number readout of each frame and interpolates between frames to artificially increase the frame rate. It then converts the digital numbers to the log-scale with a linearized region for low numbers for the comparison process and mimics the analog circuity through a low-pass filter to recreate the time delay within the circuitry. At each time step, v2e calculates the maximum number of events on each pixel, adds noise events to the event total, and then evenly subdivides the event time stamps between the frames to generate the event stream. Using the digital number representation of current poorly captures the dynamic range, and time stamp assignment creates artificial frequencies in the event data stream. These simplifications result in v2e being unable to produce representative data for SDA scenarios to access potential performance and develop algorithms. For these reasons we develop the original SDA simulation that operates on simulated photon-level information and includes a model of the arbitration process. One unmodified component in the original SDA simulation is noise event generation. In this paper, we leverage the electron-level information to inform the modeling of dark shot noise in Section 2.2 and high frequency white noise in Section 2.3. Our goal is to improve the accuracy of the time stamps and polarities of noise signatures for low-light simulation. Section 3 explores the performance of our methods compared to empirical data. Finally, Section 4 reflects on the importance of noise modeling to enable space-based EVS payloads for SDA.

2. METHODOLOGY

2.1 Simulation

The event generation simulation in Figure 1 follows v2e's processing methodology to generate events. The primary difference, we replace digital number estimates of the current with those based on the incident photo flux on the detector [21, 19]. This change reveals the true dynamic range covered by the RSOs in the scene, creating more realistic event signatures as the current changes. To calculate the flux, we introduce a front-end model to generate a representative array of the scene for each time step which includes dynamics and energy propagation. We use the SGP4 orbit propagator and observer dynamics to map between instantaneous RSOs' barycentric coordinates and ideal pixel locations [11, 26]. Then we propagate light from each RSO with an optical split-step propagation method to model the distortion during atmospheric transmission [23]. For space-based simulations, we remove the application of turbulance and assume a flat incident field at the optic's aperture. To finally estimate the induced photon flux, we take a final semi-analytical Fourier transform of the final field occluded with a mask to generate the spread of energy on the sensor [24].

Using the energy incident on each pixel, we apply a simulation framework inspired by v2e's processing but we leverage the realism of induced photocurrent working in units of amperes instead of digital numbers. Our overarching goal is to accurately simulate the camera's behavior in low-light sensing situations, such as space-based EVS. Accurate simulations capture the timings between events and their polarities in both real signals and noise. We have shown these attributes can help discriminate between sources and noise in truth data examples [20]. Accurate recreation enables exploration of space-based operational schema and algorithmic development from synthetic data to raise the probability of a space-based EVS mission success.

To capture the polarity and timing of events accurately, we simulate the processing of the induced photocurrent by the EVS hardware. First, we apply noise to the induced signal since EVS is not immune to noise in the signal. We explore new techniques to model the temporal variance in the dark current and high frequency noise in Sections 2.2 and 2.3. Next, we convert the noisy current values to a log-ampere units since the ratio of the induced and memorized current reduces to a difference in the logarithmic scale. Because the EVS circuit does not respond instantaneously to a change in photocurrent, we then model the pixel's temporal response in low light conditions by passing the current value through a low-pass filter. Subsequently, we determine if an event is recorded by comparing the difference between the low-passed induced photocurrent and the previously memorized value. If the difference yields an event, we record it in the standard address event representation output of EVS. In this simulation, the arbitration accounts for readout limits and the refractory period to avoid artificial frequencies in the event stream.

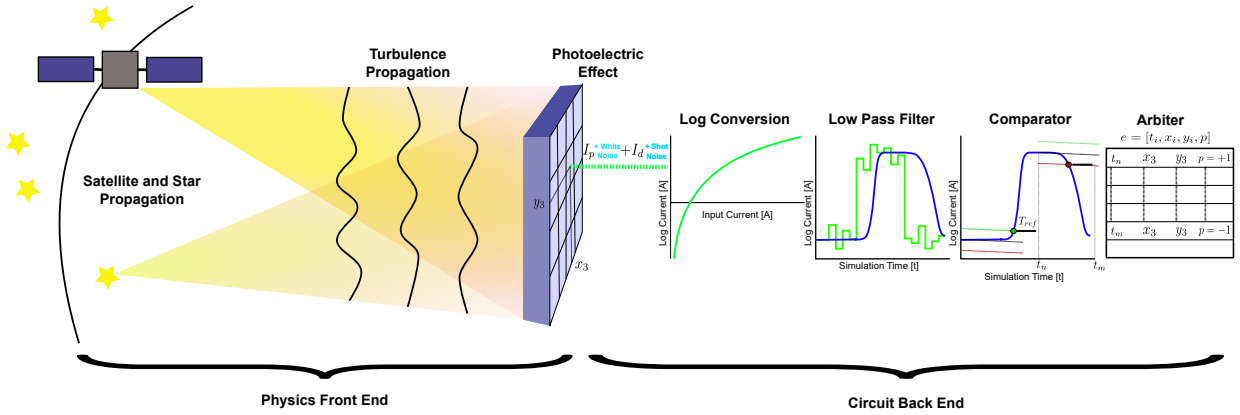

Fig. 1: The simulation is broken into two components, the physics-based front-end of the model and the circuitry-based back-end of the model. The front-end incorporates dynamics of observable objects, computes the energy sent by those objects, and propagates that energy through a simulated atmosphere. The back-end of the model encompasses the conversion to photocurrent, noise on that current, conversion to a logarithmic scale, low pass filtering the current values, comparison of the current to a memorized one, and finally arbitrating an output event stream.

2.2 Dark Shot Noise

In a typical photodiode, including those used in EVS, there is a small time-varying leakage of current over the depletion layer between the n-type and p-type layers which is called the dark current. In dark parts of the scene common in space imaging, the leakage is spread over less bandwidth and produces events. Therefore, it is important to properly capture the events generated by dark shot noise. The electron flow across the depletion layer is best parameterized as a Poisson process which produces integer numbers of electrons with non-deterministic timing. For traditional photon-level simulations, a sampling of the Possion distribution

$$P(X = k) = \frac{\lambda_e^k e^{-\lambda_e}}{k!} \tag{1}$$

defined by the electron leak rate, λ_e, over the exposure time provides sufficient temporal variation. However, there is no set exposure time to an EVS. While additional electrons flow over the photodiode, the rate at which the Poisson distribution should be sampled is not immediately clear.

There are two factors to consider. The closer the simulation time step approaches the microsecond level, the more accurate the event time stamp encoding will be. This is at direct odds with the low-pass filter imposed by the EVS circuitry. The EVS corner frequency

$$\begin{aligned} f_{3dB} &= \frac{(I_{dark} + I_{pd})}{I_{dark}} \times f_{3dBmin} \\ f_{3dB} &\leq f_{3dBmax} \end{aligned} \tag{2}$$

scales by the ratio of the pixel's induced photocurrent, I_{pd}, and dark current, I_{dark}, between the minimum, f_{3dBmin}, and maximum, f_{3dBmax}, frequencies [8, 14]. At lower induced current levels the EVS's corner frequency is close to its 1 Hz minimum. Therefore, in low-light environments, smaller time steps lower the amplitude of change imposed by a random sample taken each time step as in Figure 2a. Therefore, as the time step size decreases the less likely a threshold change occurs from the sampled Poisson distribution.

Figure 2b demonstrates this phenomenon over a 20 second simulation with a 1 fA dark current at every 2 millisecond time step and a 1 Hz corner frequency. The 2 millisecond time step is appropriate for the DAVIS346 EVS Sensor because it may be capped at a spatial change limit of 250 pixels per second for the low-light sensing of satellites and stars [14]. This simulation rate, therefore, satisfies the Shannon-Nyquist

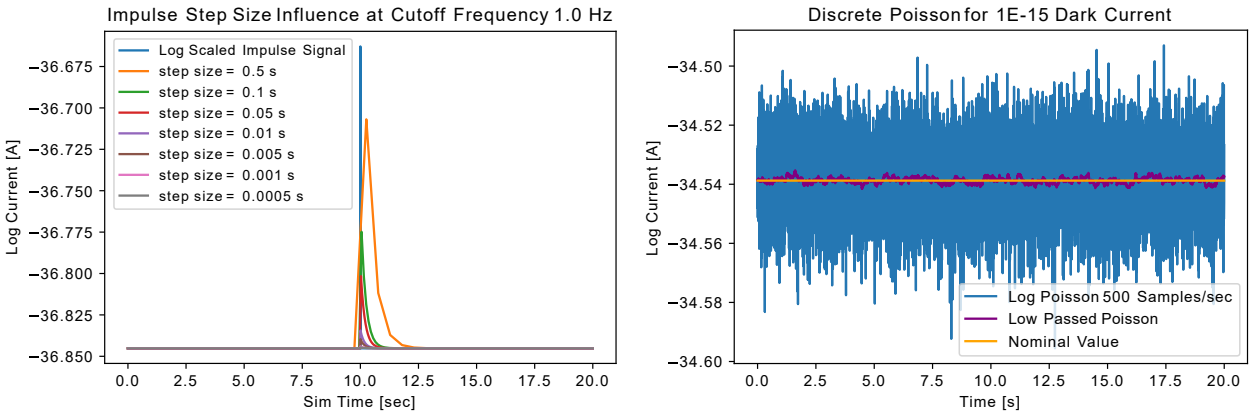

(a) Impulse response with varying step sizes

(b) Example log current with Poisson distribution

Fig. 2: Sampling a Poisson distribution conflicts with the modeling of the sensor's temporal response. The corner frequency is approximately 1 Hz at the dark current [14]. **(a)** As the step size decreases, the impulse response decreases. This decrease in the variance amplitude artificially reduces the likelihood of an event from the dark shot noise. **(b)** In practice with a Poisson taken each 2 milliseconds and a dark current of 1 fA, the low pass filter weights the previous current value 97.8%. The resulting current variance is an order of magnitude less than the original.

condition for spatial movement within the scene. In this example, the maximum current deviation from the nominal dark current decreases by approximately 70% after application of the low-pass filter. This simulation suggests that EVS operating off of instantaneous current comparisons with theoretically infinitesimally small time divisions should not experience dark shot noise, but EVS sensors are not impervious to this noise. Sensor calibration measurements taken without stimulus with the lens cap on capture dark shot noise on EVS [22]. Since dark shot noise should exist and be invariant to simulation time step size, we propose an alternative method to sample the dark current.

Theoretically, the readout of a dark current measurement is the accumulation of the total electrons crossing between the layers over the previous second. If we break a second down into smaller time steps, we have a number of electrons in each of those smaller time steps crossing between the n-type and p-type layers that contribute to the overall current. With this logic, we create an estimate of the total electrons per second at any simulation step as a summation of the electrons leaked through the photodiode over the previous second. At each time step, we sample a Poisson distribution defined by the rate of electrons per simulation time step and then sum over the samples for the previous second of simulated time. The result is an estimation of the electrons per second at the simulation time that should approximate the dark current value and, importantly, that carries the history of the previous leakage of electrons across the photodiode. We call this the rolling Poisson method.

To implement the rolling Poisson method we initialize a 3-dimensional array of random Poisson draws, with two dimensions defined by the number of sensor pixels in the x and y directions and the third defined by the number of simulation steps in a total second. Note that the simulation time step must divide one second evenly, so that the number of simulation steps in a total second is an integer. To reduce memory requirements, we replace a slice of the array at each time step. After replacing the ith slice on the ith step in an overall second of the simulation, we sum the resulting array across the time axis to get the dark current at that simulation time. At the next simulation step, we replace the $i+1$ slice. When we reach the last slice of the array, we loop back to replace the first slice. The fundamental principal behind our rolling Poisson method is maintaining consistency within the varying dark current value, inertia of the dark current, allowing for event generation despite the unfavorable temporal sampling of the simulation when compared to the low-pass filter cutoff frequency.

2.3 Photocurrent Noise

In addition to dark shot noise, other noise components include leaks within the circuitry and high frequency noise from analog components such as the source follower. The v2e simulation treats all these other noise sources under the leak rate umbrella. The commonality between leak noise generation sources is their effect on the memorized current. Through leak sources, the memorized current drops over time and eventually the logarithmic delta between the memorized current and the stable induced current reaches the θ_{ON} threshold value and produces an ON event without any change in the photocurrent required. As such, leak rate events are only ON events. To model leak noise events, our simulation and v2e assign a rate at which the leak events occur, R_{leak}. Through multiplication with the simulation time step, Δt and the threshold required to yield an ON event, θ_{ON}, they define

$$\delta_{leak} = \Delta t R_{leak} \theta_{ON} \tag{3}$$

as the change to the memorized current at each time step, δ_{leak}. They apply the change through a subtraction of δ_{leak} from the logarithmic memorized current at each time step which yields a consistent decrease. Nominally, the v2e paper [17] suggests a leak rate of 0.1 Hz is appropriate for most applications and covers both events generated by the leak through the reset switch and the parasitic photocurrent.

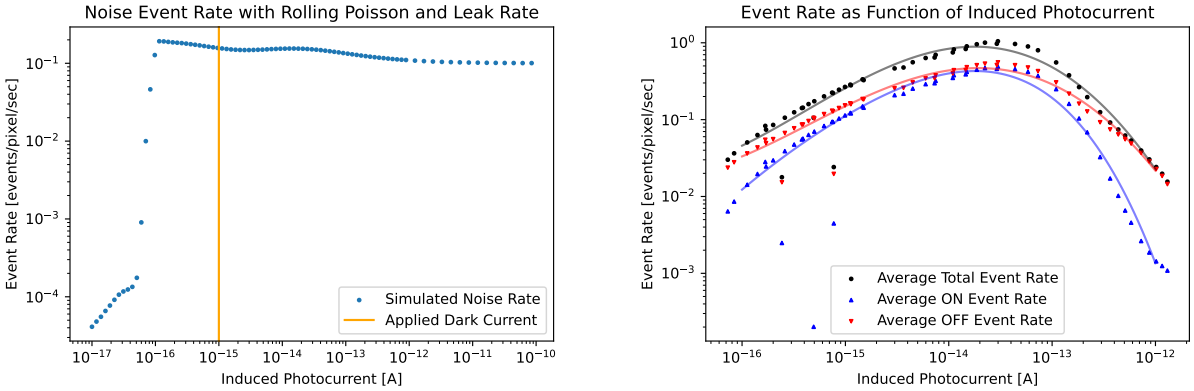

(a) Leak rate and rolling Poisson dark shot noise methods resultant event rate

(b) Experimental background noise event rates on 4th generation EVS

Fig. 3: Event noise background rate as proposed by v2e's leak rate methods does not reflect the rates and profiles of noise on pixels at given induced current values. **(a)** Modeling signal noise as a leak on the memorized photocurrent to induce a suggested 0.1 Hz rate of ON events in combination with a rolling Poisson dark shot noise model generates a discontinuous curve slightly above the leak rate when the induced current is on the same order of magnitude as the dark current. Below the dark current, the dark shot noise model dominates. Above the dark current, the leak noise rate dominates approaching the 0.1 Hz value. **(b)** Empirical data of event background rates as a function of induced photocurrent in the newest generation of sensors indicates a curve to the generated events [15]. ON and OFF events are present. These two attributes are not adequately generated by the leak rate noise model.

We apply the suggested 0.1 Hz leak rate to the rolling Poisson method with a set dark current of 1 fA over a range of induced current values. There are three distinct regions in the results, seen in Figure 3a. First, the nominal region, where the induced photocurrent is greater than the applied dark current. In this region the simulation approximately produces the nominal leak rate requested. The second region is between one decade below, and two decades above, the simulated dark current value. This region exhibits a noise event rate above the 0.1 Hz leak rate frequency. For induced photocurrents closer to and, particularly, below the dark current value, the number of events induced by dark shot noise produced by the rolling Poisson method grows. Variance above the nominal dark current triggers leak rate events earlier than the leak rate on its own, and variance below the nominal resets the memorized current to a lower value than the nominal induced photocurrent plus dark current. These two effects combine to elevate the resultant noise event rate. The final region, one decade below the dark current and lower, the induced photocurrent is no longer relevant

and the noise events are primarily driven by the dark shot noise induced by the rolling Poisson method.

While we can explain the discontinuous noise event rate generated by the v2e leak rate method and rolling Poisson method combined, Figure 3b demonstrates how erroneous the leak rate method is at producing the variation in noise events of a real EVS over a range of induced photocurrent. The empirical data in this Figure depicts events generated by a 4th generation Prophesee EVS. To create the data, the Air Force Research Laboratories subject this EVS to the constant photon flux output from an integrating sphere [15]. They collect events at varying lux levels for 60 seconds and then evaluate the overall event rate, the OFF event rate, and the ON event rate. Unlike the flat region the v2e leak rate method creates, the empirical data shows a peak noise rate at a photocurrent equivalent to the incident 4-5 lux. At both lower and higher levels of photocurrent the noise event rate drops off. It is also important to note, the OFF event rate is universally greater than the ON event rate. The v2e leak rate method only generates ON events. While the mechanism of the memorized photocurrent decreasing over time is real, the mixture of ON to OFF events in the empirical data indicates the leak noise is not a primary source of noise of events in regions of higher induced photocurrent. Therefore, we propose a new method to capture the characteristic frequencies and polarities of noise on pixels with induced photocurrent.

Our method accounts for noise sources unaddressed by the leak rate method. Components, such as the source follower introduce higher frequency noise into the EVS current. While there are possibly many contributing elements of noise within the circuitry, we apply the central limit theorem to assume we can encompass all of them with a Gaussian distribution. The Gaussian distribution about the central current value in non-log space theoretically also fits the real data noise profile of more OFF than ON events. This is because in log-space it takes less change to produce an OFF event than an ON event, a normal distribution crosses the OFF event threshold line more frequently than the ON event threshold assuming the thresholds for both polarities are equivalent. We also assume that this Gaussian noise is higher frequency because it peaks at a region of higher induced photocurrent as shown in Figure 3b and the peak may be a result of noise making it past the low-pass filter at higher induced current values. Consequently, we anticipate capturing the event rate drop-off for lower induced current values in the Figure from the Gaussian noise being modeled as high frequency. As such, we do not apply a rolling method to maintain the inertia of individual draws. Since the corner frequency does not decrease again, we expect the drop-off in the higher induced photocurrent regions is the result of the overall noise amplitude growing at a different rate than the photocurrent and becoming less consequential for high levels of current.

We use the empirical noise rate data to define the standard deviation of the Gaussian. We propose equating the area under the tails of the Gaussian probability density function, the complementary error function, to the probability of an event occurring in any simulated time step as defined by the total event rate per simulated time step. From each background event rate data set, we evaluate the noise event rate

$$E_r = \frac{e_{tot}}{x_{pix} y_{pix} t_{tot}} \tag{4}$$

by dividing the total events in a simulation, e_{tot}, by the total number of pixels, $x_{pix} \times y_{pix}$, multiplied by the total time we simulate, t_{tot}. Then we multiply by our simulation time step of 2 milliseconds to produce a probability of an event on a pixel during a unique time step. We minimize the difference

$$\arg\min\left((P_{event} - erfc(z))^2\right) = \arg\min\left(\left(P_{event} - \left(1 - \frac{2}{\sqrt{\pi}}\int_0^z e^{-t^2}\,dt\right)\right)^2\right) \tag{5}$$

between the complementary error function, erfc(z), and the probability of an event, P_{event}, squared to find the z score of the error function generating the desired area under the probability density function [10, 27]. Rearranging the z score formula to solve for the standard deviation, σ

$$\sigma = \frac{|x - \mu|}{z} \tag{6}$$

as a function of the difference between the nominal mean induced photocurrent, μ, and the photocurrent that yields an OFF threshold change, x, divided by the z score. Assuming a threshold change of 0.1 for the

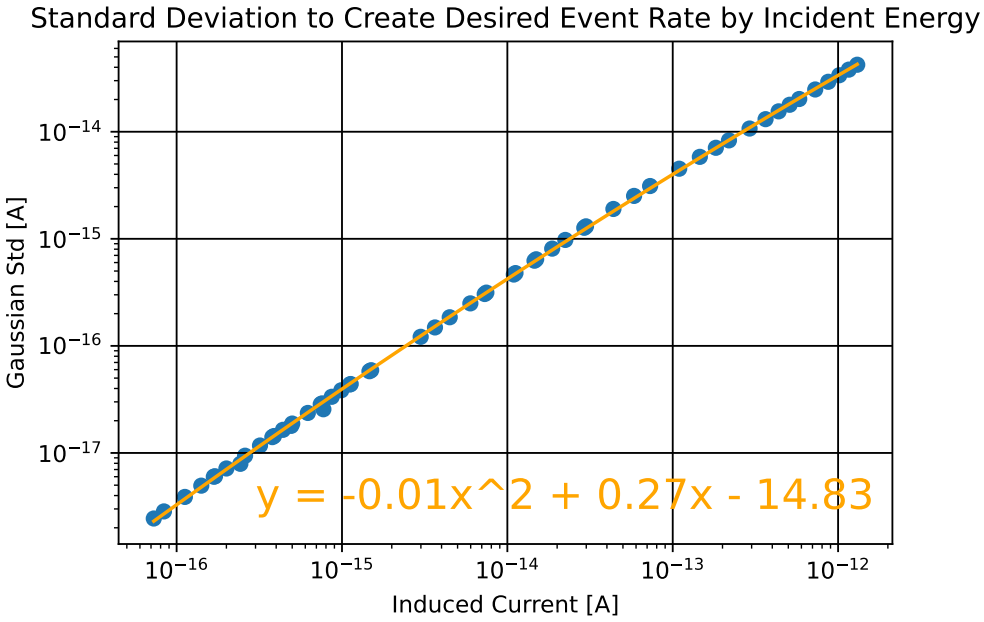

Fig. 4: The standard deviation assuming the noise event rate is the area under the Gaussian probability density function tails defines a nearly a linear relationship between the induced photocurrent and the standard deviation required to generate the expected noise events. A quadratic fit ensures a slight reduction in slope for higher values of induced photocurrent.

OFF events, we plot the Gaussian standard deviation as a function of induced photocurrent in Figure 4 on the log scale. The standard deviation to produce 0.1 threshold change is nearly 1.5 decades lower than the induced photocurrent for all values. While appearing linear, a quadratic fit captures the slight drop in the ratio between the induced photocurrent and the applied standard deviation at higher levels of photocurrent more effectively. With this continuous fit, we compute the appropriate standard deviation to sample around each pixel's induced photocurrent in the simulation at each time step.

3. RESULTS

3.1 Dark Shot Noise Analysis

Dark shot noise should be the dominant producer of noise in the dark regions between RSO sources. Therefore, producing consistent and realistic dark shot noise is a priority for the simulation. With the rolling Poisson method, a dark current must be provided for each simulation. Choosing a current is not a trivial task; in particular, the noise event rate is temperature dependent as shown in Figure 5. This Figure depicts the noise event rates we extract from 3rd Generation Prophesee sensor SDA data sets with true signals removed. The variation in these data sets are over two orders of magnitude, but there is a trend of decreased event rates with higher temperatures. Since the dark current is proportional to temperature, lower temperatures yield lower electrons leaking over the photodiode. In traditional electro-optical sensing, this is desirable. However, with EVS, smaller dark currents require less variation in the leaking electrons to yield events. Therefore, lower temperatures have higher event rates. Since the temperature dependence is so variable, we cannot choose a static setting for the dark current or a rate parameter and expect it to produce a realistic event stream. I, instead, relate the temperature at the time of the observation to the dark current and apply our rolling Poisson method.

Figure 6 demonstrates the difference between standard Poisson sampling at each time step and the rolling Poisson method. Using the same experimental conditions and random seed as Figure 2b, the resulting dark current at each simulation step varies around the nominal dark current of 1 fA and maintains more variance

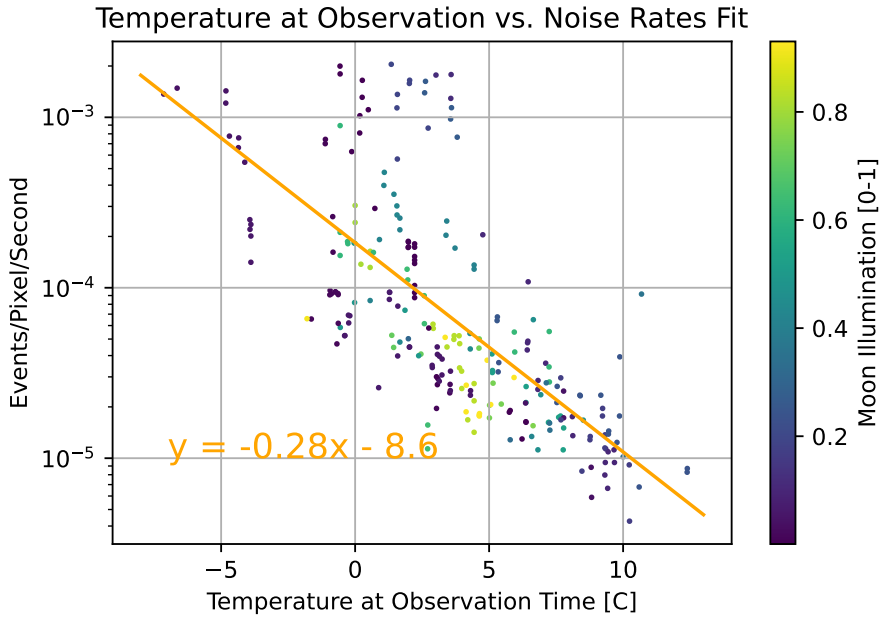

Fig. 5: Temperature at time of measurement plotted against the noise rate, excluding hot pixels, with a fit linear relationship between the temperature and logarithmic noise rate. The moon illumination, captured in the color scaling of the points, demonstrates the lack of correlation between the moon phase and background noise event rate generated.

through the low-pass filtration process. In this one pixel example, the maximum variation off the nominal log dark current due to a rolling Poisson method is 49.2% less than the maximum variation from the normal Poisson sampling. While this may seem concerning because the goal is to induce occasions when a threshold change occurs on the log scale, the inverse is true on the low-passed maximum variation due to the enforced inertia. After the low-pass filter, the standard Poisson sampling method maximum is 81.2% less than the rolling Poisson method. It is also important to understand the resulting density of current values away from the nominal dark current. Assuming normality, one standard deviation from the nominal log current value is approximately 16% less than with the traditional sampling method. Again, this statistic inverts after the low-pass filter with an 89.6% reduction in the standard deviation between the rolling Poisson and traditional methods. This follows the order of magnitude lost in the current variation that Figure 2b highlights. In fact, comparing the change in the standard deviation before and after the low-pass filter, the traditional Poisson method has a 92.1% loss and the rolling Poisson method has only a 10.4% loss. These statistics confirm the efficacy of the inertia theory behind the rolling Poisson method to create deviations far enough from the dark current to yield events.

While the previous simulation captures the effectiveness of inertia in the dark current methods, the number of current samples is too small for the method with inertia to effectively evaluate if the resulting distributions resemble Gaussian distributions. Increasing the number of time steps sampled to 100,000, Figure 7a depicts the traditional Poisson sampling method as the baseline distribution expectation besides the scale on the low-passed distribution. Given the sampling rate is in the 1000s of electrons per second, the Poisson sampling creates a Gaussian distribution of current values. The co-location of the mean and median and the Fisher excess kurtosis and skew metrics being close to 0 confirm the Gaussian distribution. The larger number of samples minimally affects the loss statistics for the traditional Gaussian. Both the standard deviation and the maximum variation reduce by 92% through the application of the low pass filter as they did with the shorter simulation. The effective concentration at values closer to the mean make it a more leptokurtic distribution.

As Figure 7b indicates, with enough samples, the rolling Poisson method forms a Gaussian distribution.

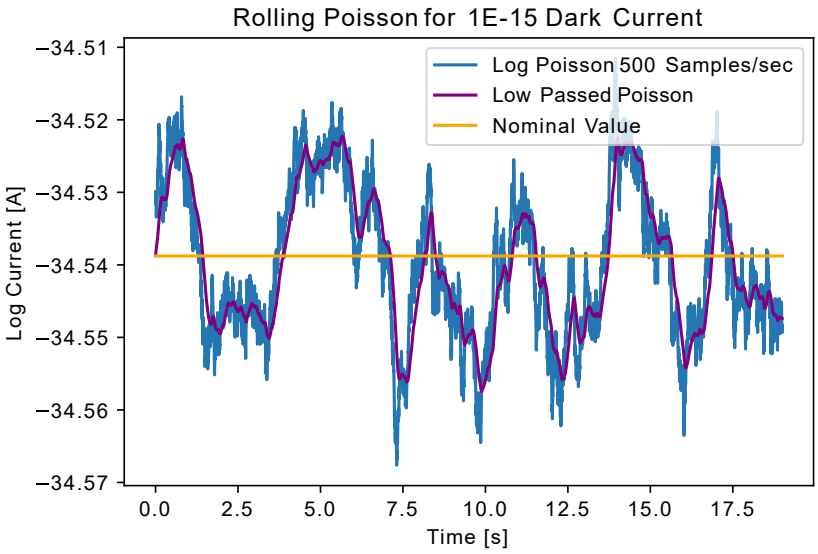

Fig. 6: The rolling Poisson method in practice ensures the deviation of the current from the nominal current value has enough inertia to allow the deviations through the low pass filter. The loss in the current standard deviation is only 10% as opposed to the 93% loss for the simulation run with standard Poisson sampling.

The mean and the median are co-located and the excess Fischer kurtosis and skew are on the same order of magnitude as the traditional Poisson method. For further assurance, we check the normality of the low passed rolling Poisson distribution using the Kolmogorov-Smirnov test for goodness of fit [9, 18]. In this test, we check for agreement with the null hypothesis, the distribution is normal. Using a 95% confidence interval, the resulting p-value of 0.7 is greater than 0.05 and, therefore, the rolling Poisson distribution is consistent with the null hypothesis. Now that I've verified the normality of the rolling Poisson distribution, we compare the standard deviation of the current with the traditional Poisson sampling method's standard deviation. With more samples, the difference in the standard deviations reduces from 16% to only 5.4%. While the differences in the current standard deviations tighten with more samples, the distribution also highlights the rolling Poisson's co-located mean and median are slightly displaced from the nominal 1 fA at a value of approximately 9.98E-16A, a 0.004% difference from the nominal. This displacement is a result of the subdivided Poisson rate summation. At the 2 millisecond simulation step size, the 1000s of electrons per second equates to single digit rates of electrons per time step, so the distribution acts less Gaussian and more Poisson. The larger sample size of this second test not only allows for distribution testing but provides more insight on the expected affect of the low-pass filter on the dark current values. In particular, the reduction in the standard deviation, capturing the overall affect of the low-pass filter, reduces to 7.5% from 10.4% with the larger sample size. In total, the rolling Poisson maintains the expected normality while enabling the magnitude of the variance to pass through the low pass filter, verifying the method provides the desired affect on the simulation.

At a pixel level, the rolling Poisson method provides the desired effect of maintaining the dark current variation through the low-pass filter while maintaining the expected distribution characteristics. One additional benefit of this method is that there are only two parameters that influence the dark shot noise event generation rate: the dark current and the threshold values. No tuning of a sampling rate is needed. Taking a closer look at the dark current parameter, the dark current value determines the electron rate that defines the sampled Poisson distribution. At lower levels of dark current, the number of time steps without any electrons leaking between the photodiode layers increases. This increase drives the rolling Poisson summation further from the nominal value. In addition, since the comparison to generate an event is a ratio of the actual current and the memorized current, as the dark current value decreases, the amount of current variation required to generate an event decreases. We purely vary the dark current values for a set threshold of 0.1 on a 480 by 640 array during a 20 second simulation in Figure 8a. The compounding factors of less variation occurring and more variation required to generate an event produces a quadratic drop-off in the

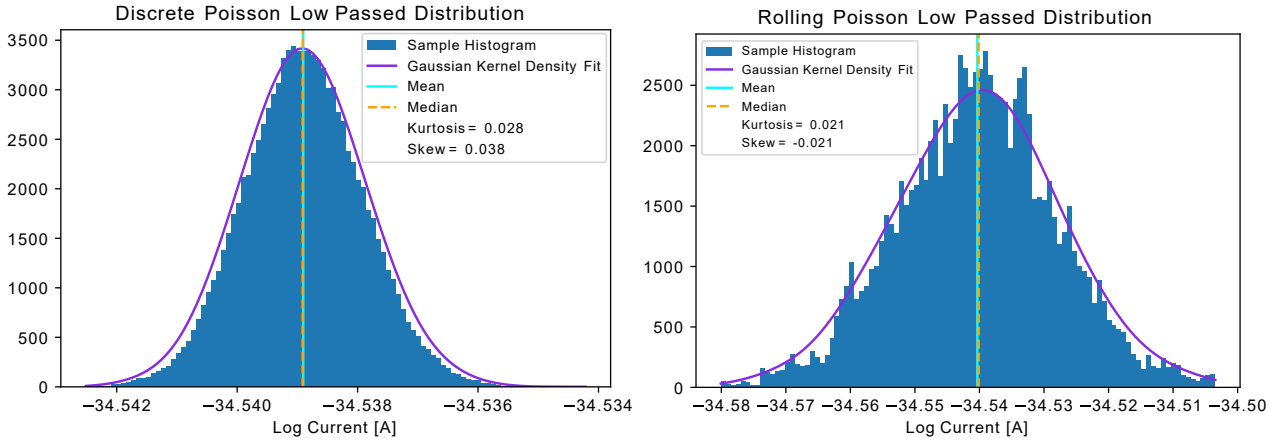

(a) Traditional discrete Poisson distribution

(b) Rolling Poisson method distribution

Fig. 7: Distributions of the traditional and rolling Poisson sampling methods over 100,000 samples at a estimated dark current of 1 fA demonstrates that both resulting distributions are Gaussian. **(a)** The rate parameter for the traditional Poisson is in the 1000s of electrons per second so it creates an effectively Gaussian distribution; The mean and median are co-located at the actual dark current value of 1 fA and the Fischer kurtosis and skew metrics are nearly 0. The kurtosis increases slightly after the low-pass filter, becoming more leptokurtic. Due to the low-pass filter the magnitude of the standard deviation decreases 92.2% effectively matching the simulation with fewer samples. **(b)** A more cohesive distribution of current values is visible after sampling 100,000 time steps with the rolling Poisson distribution. The resulting mean is 9.98E-16, 0.004% away from the nominal dark current of 1 fA. Despite this slight offset, the distribution is promisingly Gaussian; the mean and median are co-located and the kurtosis and skew metrics remain consistent through the low-pass filter at values close to 0. Like the traditional Gaussian sampling the final distribution is slightly leptokurtic.

noise event rate as the dark current increases. This follows the behavior of the empirical data in Figure 5 where as the dark current increases with temperature, the noise rate decreases.

Next, we simulate the threshold to event relationship with a 1 fA dark current over the same 480 by 640 pixel array and 20 seconds of simulation time while only varying the thresholds, shown in Figure 8b. It follows as the threshold decreases the number of samples in the tails of the distribution resembles the complementary error function evaluated at increasingly smaller values of z. In the limit where $z = 0$, every pixel generates an event at its maximum frequency, typically limited by the chosen refractory period or the sensor readout when the refractory period is short. This relationship supports higher thresholds being a significant tool to limit the dark shot noise event generation. The trade-off is decreased sensitivity to weaker point sources, a common issue with EVS SDA applications [14, 13]. The drop-off in the dark shot noise event rate is a quadratic function with respect to the threshold value. For this application, an optimum bias setting may exist between the dark shot noise event suppression and weak source event generation. This optimum could best be found with improved knowledge of the dark current and control of the external parameters such as temperature affecting the dark current to ensure consistent performance.

3.2 Signal Noise Analysis

Regions of the focal plane where the dark current and, therefore, dark shot noise do not dominate the current, are instead dominated by current leakage and high frequency noise. We apply the high frequency Gaussian fit method to a 480 by 640 array for 20 seconds of simulation time assuming a threshold of 0.1, a dark current of 1 fA, and a corner frequency of 2.5 Hz. We evaluate the noise event rates for ON and OFF events separately and combined. Figure 9 plots these rates as a function of the induced photocurrent for each simulation. Unequivocally, the Gaussian fit method produces a more realistic noise event rate than the leak rate method in Figure 3a. First, the noise generated produces both ON and OFF events instead of only ON events. While the simulation always produces more OFF events, like the empirical data, the

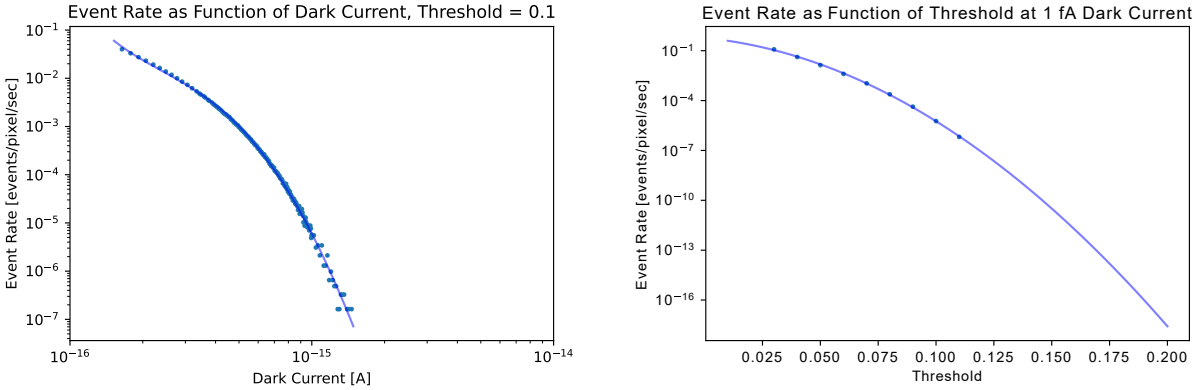

(a) Dark current influence on dark shot noise

(b) Threshold bias settings on dark shot noise

Fig. 8: The event rate the rolling Poisson method generates is a function of the dark current and the threshold value. **(a)** As the dark current increases the event rate attributable to the dark shot noise decreases. The response of the event rate to tuning this parameter is a quadratic drop-off in the log space of both the dark current and the noise event rate. Within smaller regions of performance, to match the temperature of a measurement, a linear fit is sufficient. **(b)** The dark shot noise event rate generation is closely tied to the threshold bias selection and amounts to increased area in the tails of the complementary error function. Choosing a higher threshold limits the dark shot noise generated, but will also limits the sensitivity of the sensor to weak signal sources.

ratio of ON and OFF events benefits from the quadratic fit of the standard deviation. The largest standard deviation with respect to the induced photocurrent occurs at the peak in the curvature of the quadratic fit. The larger relative standard deviation provides more opportunities for ON events as a greater portion of the distribution in the tails passes the ON threshold. Consequently, as the fit moves away from that peak, the ON events decay faster than the OFF events. In those regions the noise OFF events dominate. Inspection of the empirical data also indicates this phenomenon.

Besides the magnitude of the overall noise event rates generated, which differ from the empirical data due to the size of the array modeled, the decay of the noise event rate at lower induced photocurrent levels does not follow the empirical data's trend of decay over a couple decades of photocurrent values. We attribute the sharp decline in events to the change in the frequency cutoff in that region. The corner frequency following the proportional relationship in Equation 2 grows by roughly an order of magnitude per decade above the nominal dark current and the original corner frequency until reaching 3 kHz. With these simulation parameters, the simulation reaches the maximum corner frequency at approximately 1E-12 A. The issue in the simulation could simply be that the maximum corner frequency should be reached at a lower induced current value, which would extend the influence of the high frequency Gaussian fit into lower induced current values. Working with the originally proposed proportional relationship, either a greater low end corner frequency or a dark current less than 1 fA will move the initial maximum corner frequency to the left. In this simulation, the dark shot noise event rate requires a threshold around 0.1 to produce the dark shot noise event rates observed in the empirical data while the default threshold bias value is around 0.2. Alternatively, the proportional relationship defining the slope of the corner frequency may be more complex than originally anticipated. While we can currently work around this issue through manipulation of the dark current value, experimentation through empirical measurements of the dark current and simulations with alternative corner frequency functions will clarify the underlying cause of the rapid decay from the high frequency noise.

Since the output of the simulation is a full event data stream, we go a step further than magnitude of event generation to evaluate the performance of the high frequency Gaussian noise. With the data stream of events, we subdivide the time series of event data into distinct time subsets and evaluate the event rate within the subdivisions to ascertain the consistency and frequency of the noise event occurrence. Working with the

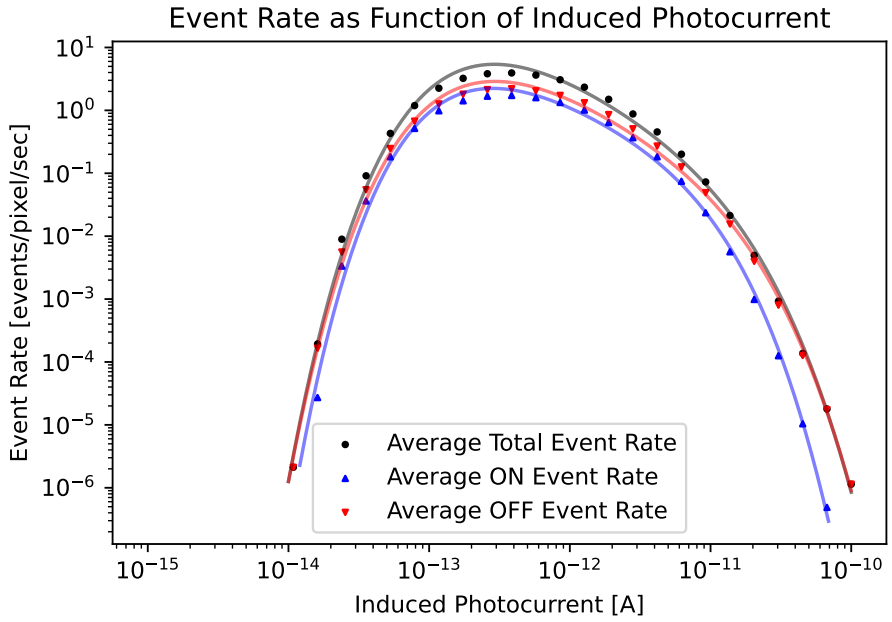

Fig. 9: The quadratic fit of the required Gaussian standard deviations to implement as high frequency noise produces many of the attributes in the empirical data. First, the event rate peaks at a mid-range photocurrent value and drops-off towards higher and lower induced photocurrents. The OFF event rate is the primary source of events throughout the simulation with a more equal distribution of ON and OFF events in the regions with the highest event rates. The one unanticipated effect is the steep drop-off of events one decade above the dark current. This steep decline may be indicative of an incorrectly selected dark current for this simulation or a need to further refine the cutoff frequency relationship to dark current and induced photocurrent.

empirical data first, Figure 10a depicts the distribution of event rates normalized as a density function over multiple time step intervals. For each time subdivision, the resulting distribution has a positive skew with the median at a slightly lower rate than the mean. The mode deviates more, especially at the largest step sizes, because there are only a few time step samples and they may all be unique despite being close in value. As the step size decreases the density of the distribution widens gaining more negative kurtosis, becoming platykurtic. The broadening of the distribution indicates a larger variation in the smaller time increments. The smoothness of the distribution at the smaller time increments indicates a fairly consistent rate of event generation.

In comparison, Figure 10b highlights that at the macroscale the high frequency tuned Gaussian method produces a positively skewed distribution of events just like the empirical data. The rate is not directly comparable because we simulate the 3rd generation Prophesee EVS which has a different pixel count, scaling the noise event rate. Additionally, the sensor itself is expected to have different noise performance. Therefore, we do not select the two induced photocurrents in Figures 10a and 10b to match but to highlight the overall noise behavior. As we decrease the time increment for the synthetic data, the positively skewed distribution breaks down into multiple clusters of event rates instead of becoming a broad platykurtic distribution. This occurs at time increments on the same order of magnitude as the simulation step size, 2 milliseconds. This behavior indicates the generation of events within a simulation step are being clustered together. Currently, we assign the time stamp when the threshold is reached assuming a linear interpolation between the starting and ending induced logarithmic current and a memorized current leak. The arbitration process can modify this time stamp when there is a backlog of events. However when not overloaded, the linear assumption determining the event trigger times of events is applying its own frequency and is erroneous. We recommend modification of the event trigger time determination method to be a linear change in the non-log current scale

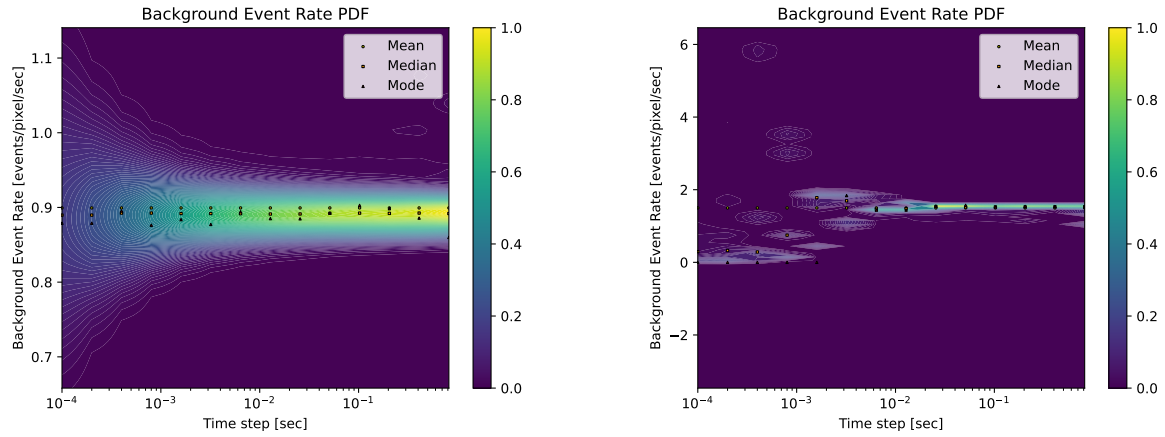

(a) Event rate distribution at different time subdivisions on empirical data

(b) Event rate distribution at different time subdivisions on synthetic data

Fig. 10: Subdivision of the event time series into temporal bins to calculate event rates throughout the collections and fit to a probability density function demonstrates a discrepancy in event time stamps between the empirical and simulated data sets. **(a)** The empirically collected noise event time series demonstrates the consistent spread of the noise event generation when an EVS sensor is subjected to consistent incident energy. The distribution has a positive skew for all time subdivisions and the distribution grows further platykurtic as the time steps decrease. The distribution's smoothness at the smallest time divisions indicates consistent event generation without additional underlying frequencies. **(b)** The synthetic noise event time series demonstrates a less consistent spread of events than the empirical data. Up to the time steps on the same order of magnitude of the simulation time steps, 2 milliseconds, the distribution has a positive skew for all time subdivisions and begins its broadening of the noise event rate. However, at smaller subdivisions, the event rates generated do not share the smoothness seen in the empirical data. The binning is indicative of the event trigger times being weighted towards one side of the time step. Refinement of the time stamp method is necessary to remove the artificially imposed frequency.

as opposed to being evaluated in the log scale as it is now. This modification is required before generation of synthetic data with reliable frequency information is possible through our simulation methods. It applies to all changes in current, not just noise, the noise rate analysis just highlights the impact of the interpolation method.

One final aspect we examine in the synthetically generated noise data returns to the macro-scale generation of overall event rates. We wish to find the time of a simulation required to get a reliable noise event rate value for future simulation runtime optimization. The empirically collected data sets are each 60 seconds long and our simulated noise data sets are 20 seconds long. We evaluate the total event rate after each new event in each data set, which provides an estimate of the total event rate over time. The noise event rate as a function of the simulation time, as in Figure 11a, typically has an initial spike from the first few events happening early in the time history, a period of underestimation, and then a rise to the nominal noise event rate as the simulation length increases. For the data set in this Figure, the estimate is within 90% of the final event rate at approximately 2.5 seconds and 1.5 million events.

Figure 11b depicts both the relationship between the number of events and the total time to reach the settling threshold as a function of the total number of events in a data set. For data sets with higher event rates and, therefore, more total events output from the 20 seconds simulated, the number of events to reach the 90% of the final estimate plateaus at 1.5 million events. Therefore, there are diminishing returns to generating longer data sets when the anticipated noise event rate is high. For lower event rate data sets, the relationship between the total number of events and the 90% convergence is more linear with approximately 88% of the events needed to settle. The deviation for data sets at and below 100 events indicates longer simulation times are required to accurately capture the noise event rates. This is further reiterated by the

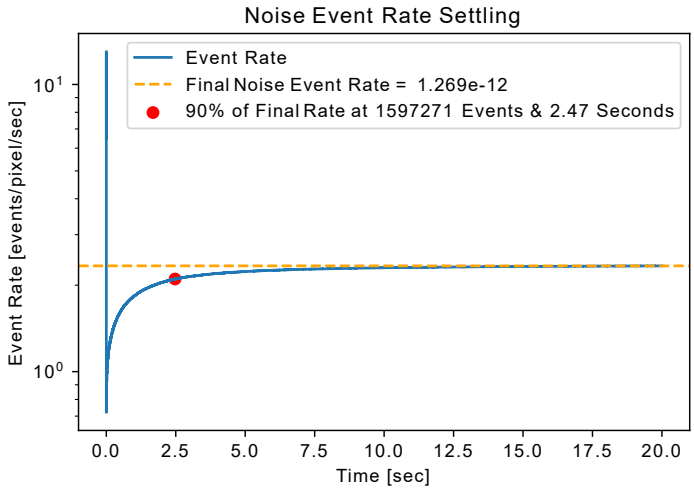

(a) Example event rate settling profile

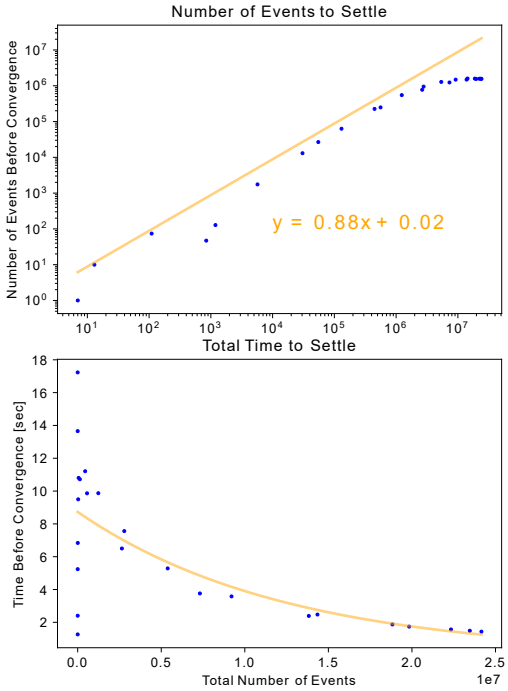

(b) Number of events and time to settle as a function of total events

Fig. 11: The event rate trend as a function of simulation duration demonstrates a relationship of the total simulation time and number of events for the event rate to converge on a final value. **(a)** By evaluating the total event rate after each new event, we extract the rise time to the final noise event rate from the time series data. The red dot indicates the time the noise event rate is within 90% of the nominal value. **(b)** The number of events to reach 90% of the final reported event rate as a function of the total number of events demonstrates the advantage of a large number of event samples. The largest data sets plateau for convergence around 1.5 million events. The simulation time to reach 90% of the final reported event rate as a function of the total number of events demonstrates an exponential decrease in convergence time as the total number of events grow. Data sets with low numbers of events do not follow this trend further supporting the conclusion of more information is required for convergence.

total time to settle as a function of the total number of events. The data sets in the 100s of events range do not fit the exponentially decreasing curve and probably do not have enough events within the 20 second simulation to prove convergence of their noise event rate. Therefore, in future noise analyses, we recommend tailoring the length of simulations by the number of samples generated instead of a fixed simulation time.

In summary, the high-frequency Gaussian with a tuned standard deviation proves promising as a method to properly mimic the noise event generation of EVS sensors in simulation. At a macro-level, the method captures many characteristics in the empirical data: the peak noise event rates and drop-off at higher current levels, the use of a Gaussian distribution creates a realistic stronger preference to OFF events than ON events, and the distribution of events demonstrates the positive skew of the larger time increments. The distribution analysis, however, highlights a need to revisit the relationship between the frequency cutoff and the determination of event trigger time between simulation time steps.

4. CONCLUSIONS

There are two main sources of noise we modify in the EVS SDA simulation: dark shot noise and high frequency noise. Each require a new methodology to fully leverage the electron per second flux information provided from the radiometric portion of the model. Ideally, from leveraging this information, the noise

generated mimics the behavior of EVS noise event generation. Properly capturing the timing and polarities of noise events in the synthetic data will enable realistic simulation of space-based EVS operations to inform system and algorithm development.

For the dark shot noise, we identify a trade-off between high temporal sampling required to capture spatial motion through the array and passing randomly sampled noise through the low-pass filter. In order to maintain the temporal sampling we desire in the overall simulation and still yield dark shot noise events, we develop a rolling Poisson summation method to track the effective dark current at each simulation time step. With the history of the previous time steps, up to one second of draws, the dark current retains some inertia from the previous time steps. Since it does not rapidly change, the dark current variation maintains a greater amplitude from the nominal dark current than a traditional Poisson sampling at each time step. With enough time steps, we prove the resulting simulation has the same qualities in the resulting distribution as the traditional Poisson method. On the macro-scale, our rolling Poisson method event rates are on the same order of magnitude as those extracted from the empirical data. One great advantage of our new method is the minimal parameter space to implement it properly. We only need an estimate of the dark current and the change thresholds of the EVS in order to apply this method. With its simplicity and effectiveness, the rolling Poisson method now is the method of choice within the EVS simulation.

Next, we address the deficiency found in modeling high rate noise only through the leak rate process. The previously implemented leak rate process only produces ON events and the rate of events is uniform regardless of induced photocurrent. Inspired by background noise curves for EVS sensors, we apply a tuned Gaussian method setting the noise event rate per simulation step as the probability under the tails of a Gaussian curve. After conversion to a standard deviation to produce that rate, we apply the quadratic trend to determine the standard deviation of the Gaussian taken at each time step. The result has remarkable similarities to the original background noise curve. There is a peak noise event rate in the middle of the induced photocurrent we simulate and a drop-off at both higher and lower photocurrent. The Gaussian, tuned to the lower end threshold to define the required standard deviation, produces more OFF events than ON events which is another characteristic observed in the empirical data.

Despite these successes, the results highlight two changes that must be made to the simulation in order to capture the right frequency of noise events at lower photocurrent, levels relevant to SDA information, and achieve the goal of synthetic event time series with accurate frequency information. First, the high-frequency Gaussian method is particularly susceptible to the drop-off of the cutoff frequency from approximately 3000 to 1 hertz. With the current model, the cutoff frequency effectively scales by an order of magnitude for each decade of photocurrent. It is not evident with currently available information if the cause of modeled noise event rate drop-off is simply an overestimation of the dark current frequency or if the equation defining the frequency cutoff is erroneous. Dark current measurements and study of the frequency cutoff may be required to answer this open question. The other simulation issue we identify during the event rate per simulation step analysis is an unintended imposed frequency in the event readout. We theorize the clustering of events into common rate bins is tied to the event trigger times being assigned improperly. The current method applies linear interpolation in the log scale. We suggest the modification of this method to impose linear change between photocurrents in the non-log scale and a subsequent timing analysis to verify the correction method.

In summary, our proposed methods of noise event generation both utilize the electron-level information about the circuit and create noise event rates on the order of magnitude with correct polarity statistics and distribution types. These methods are a major advancement in synthetically replicating low-light EVS behavior, providing a tool to model operations and test algorithms that move EVS one step closer to space-based SDA applications.

5. REFERENCES

[1] Saeed Afshar, Andrew Peter Nicholson, Andre Van Schaik, and Gregory Cohen. Event-based object detection and tracking for space situational awareness. *IEEE Sensors Journal*, 20(24):15117–15132, 2020.

[2] Samya Bagchi and Tat-Jun Chin. Event-based star tracking via multiresolution progressive hough

transforms. In *Proceedings of the IEEE/CVF Winter Conference on Applications of Computer Vision*, pages 2143–2152, 2020.

[3] Jeffery Bloch, Lynda Liptak, David Briscoe, Suzzanne Falvey, and Tasha Adams. AURORAS: The Next Evolution of Orbit Determination Using Passive Optical Observations. In *Proceedings of the Advanced Maui Optical and Space Surveillance (AMOS) Technologies Conference*, September 2022.

[4] Brian Cheung, Mark Rutten, Samuel Davey, and Greg Cohen. Probabilistic multi hypothesis tracker for an event based sensor. *IEEE Sensors Journal*, 20:15117–15132, December 2020.

[5] Tat-Jun Chin, Samya Bagchi, Anders Eriksson, and Andre Van Schaik. Star tracking using an event camera. In *Proceedings of the IEEE/CVF Conference on Computer Vision and Pattern Recognition Workshops*, pages 0–0, 2019.

[6] Gregory Cohen, Saeed Afshar, Brittany Morreale, Travis Bessell, Andrew Wabnitz, Mark Rutten, and André van Schaik. Event-based sensing for space situational awareness. In *Proceedings of the Advanced Maui Optical and Space Surveillance (AMOS) Technologies Conference*. Maui Economic Development Board, September 2017.

[7] Gregory Cohen, Saeed Afshar, and André Van Schaik. Approaches for astrometry using event-based sensors. In *Advanced Maui Optical and Space Surveillance (AMOS) Technologies Conference*, page 25, 2018.

[8] Tobi Delbruck, Yuhuang Hu, and Zhe He. V2e: From video frames to realistic dvs event camera streams. *arXiv e-prints*, pages arXiv–2006, 2020.

[9] SciPy developers. Two-sample kolmogorov-smirnov test. `https://docs.scipy.org/doc/scipy/reference/generated/scipy.stats.ks_2samp.html`, 2023. Accessed 31-07-2024.

[10] Walter Gautschi. Efficient computation of the complex error function. *SIAM Journal on Numerical Analysis*, 7(1):187–198, 1970.

[11] Felix R Hoots, Paul W Schumacher Jr, and Robert A Glover. History of analytical orbit modeling in the u.s. space surveillance system. *Journal of Guidance, Control, and Dynamics*, 27(2), March 2004.

[12] Matthew G McHarg, Richard L Balthazor, Brian J McReynolds, David H Howe, Colin J Maloney, Daniel O'Keefe, Rayomand Bam, Gabriel Wilson, Paras Karki, Alexandre Marcireau, et al. Falcon neuro: an event-based sensor on the international space station. *SPIE Optical Engineering*, 61(8), August 2022.

[13] Peter N McMahon-Crabtree and David G Monet. Commercial-off-the-shelf event-based cameras for space surveillance applications. *Applied Optics*, 60(25):G144–G153, September 2021.

[14] Brian McReynolds, Rui Graca, Rachel Oliver, Masashi Nishiguchi, and Tobi Delbruck. Demystifying Event-based Sensor Biasing to Optimize Signal to Noise for Space Domain Awareness. In *Proceedings of the Advanced Maui Optical and Space Surveillance (AMOS) Technologies Conference*, page 142, September 2023.

[15] Brian J McReynolds, Rui Graca, Lucas Kulesza, and Peter McMahon-Crabtree. Re-interpreting the step-response probability curve to extract fundamental physical parameters of event-based vision sensors. In *Unconventional Optical Imaging IV*, volume 12996, pages 127–140. SPIE, 2024.

[16] Yonhon Ng, Yasir Latif, Tat-Jun Chin, and Robert Mahony. Asynchronous kalman filter for event-based star tracking. In *European Conference on Computer Vision*, pages 66–79. Springer, 2022.

[17] Yuji Nozaki and Tobi Delbruck. Temperature and parasitic photocurrent effects in dynamic vision sensors. *IEEE Transactions on Electron Devices*, 64(8):3239–3245, August 2017.

[18] U.S. Department of Commerce. Kolmogorov-smirnov goodness-of-fit test. `https://www.itl.nist.gov/div898/handbook/eda/section3/eda35g.htm`, 2023. Accessed 31-07-2024.

[19] Rachel Oliver. *An Event-Based Vision Sensor Simulation Framework for Space Domain Awareness Applications*. PhD dissertation, Cornell University, 2024. forthcoming.

[20] Rachel Oliver, Brian McReynolds, and Dmitry Savransky. Event-based sensor multiple hypothesis tracker for space domain awareness. In *Proceedings of the Advanced Maui Optical and Space Surveillance (AMOS) Technologies Conference*, September 2022.

[21] Rachel Oliver and Dmitry Savransky. Event-based sensor model for space domain awareness. In *Proceedings of the Advanced Maui Optical and Space Surveillance (AMOS) Technologies Conference*, September 2021.

[22] Seth Roffe, Himanshu Akolkar, Alan D George, Bernabé Linares-Barranco, and Ryad B Benosman. Neutron-induced, single-event effects on neuromorphic event-based vision sensor: A first step towards space applications. *IEEE Access*, May 2021.

[23] Jason D Schmidt. *Numerical Simulation of Optical Wave Propagation with examples in MATLAB*. SPIE, 2010.

[24] Remi Soummer, Laurent Pueyo, Anand Sivaramakrishnan, and Robert J Vanderbei. Fast computation of lyot-style coronagraph propagation. *Opt. Express*, 15, Nov 2007.

[25] Luc Tinch, Nitesh Menon, Keigo Hirakawa, and Scott Mc-Closkey. Event-based Detection, Tracking, and Recognition of Unresolved Moving Objects. In *Proceedings of the Advanced Maui Optical and Space Surveillance (AMOS) Technologies Conference*, September 2022.

[26] David A Vallado, Paul Crawford, Richard Hujsak, and TS Kelso. Revisiting spacetrack report #3: Rev 2. *AIAA*, 2006.

[27] Mofreh R Zaghloul and Ahmed N Ali. Algorithm 916: computing the faddeyeva and voigt functions. *ACM Transactions on Mathematical Software (TOMS)*, 38(2):1–22, 2012.

[28] Michał Zołnowski, Rafal Reszelewski, Diederik Paul Moeys, Tobi Delbruck, and Krzysztof Kamiński. Observational evaluation of event cameras performance in optical space surveillance. In *NEO and Debris Detection Conference, Darmstadt, Germany*. ESA Space Safety Programme Office, 2019.